Observations of metallic species in Mercury's exosphere

Rosemary M. Killen [a,*], Andrew E. Potter [b], Ronald J. Vervack Jr. [c], E. Todd Bradley [d], William E. McClintock [e], Carrie M. Anderson [a], Matthew H. Burger [a]

[a] NASA Goddard Space Flight Center, Greenbelt, MD 20771, United States
[b] National Optical Astronomy Observatory, Tucson, AZ 85719, United States
[c] The Johns Hopkins University Applied Physics Laboratory, Laurel, MD 20723, United States
[d] Department of Physics, University of Central Florida, Orlando, FL 32816, United States
[e] Laboratory for Atmospheric and Space Physics, University of Colorado, Boulder, CO 80303, United States

ARTICLE INFO

ABSTRACT

From observations of the metallic species sodium (Na), potassium (K), and magnesium (Mg) in Mercury's exosphere, we derive implications for source and loss processes. All metallic species observed exhibit a distribution and/or line width characteristic of high to extreme temperature – tens of thousands of degrees K. The temperatures of refractory species, including magnesium and calcium, indicate that the source process for the atoms observed in the tail and near-planet exosphere are consistent with ion sputtering and/or impact vaporization of a molecule with subsequent dissociation into the atomic form. The extended Mg tail is consistent with a surface abundance of 5–8% Mg by number, if 30% of impact-vaporized Mg remains as MgO and half of the impact vapor condenses. Globally, ion sputtering is not a major source of Mg, but locally the sputtered source can be larger than the impact vapor source. We conclude that the Na and K in Mercury's exosphere can be derived from a regolith composition similar to that of Luna 16 soil (or Apollo 17 orange glass), in which the abundance by number is 0.0027 (0.0028) for Na and 0.0006 (0.0045) for K.

Published by Elsevier Inc.

1. Introduction

We present observations of the metallic species sodium (Na), potassium (K), and magnesium (Mg) in Mercury's exosphere. Although sodium and potassium have been observed previously from ground-based platforms (e.g., Potter et al., 2002), we present a map of the Na/K abundance ratio over the observed sunlit disk of the planet. Magnesium was discovered in Mercury's exosphere during the second flyby of the innermost planet by the MErcury Surface, Space ENvironment, GEochemistry, and Ranging (MESSENGER) spacecraft (McClintock et al., 2009). Here, we present an analysis of the observed Mg column abundances and a discussion of the implications for source and loss processes. All metallic species observed exhibit a distribution and/or line width characteristic of high to extreme temperature. The temperatures of refractory species, including magnesium (Mg) and calcium (Ca), indicate that the source process for the atoms observed in the tail and near-planet exosphere are consistent with ion sputtering and/or impact vaporization of a molecule with subsequent dissociation into the atomic form. The very high energy metallic species may indicate that a resonance process of some kind is acting to produce a highly energetic gas that may not be thermal. We discuss the results in the context of assumed surface composition, and we assess the source and loss processes as constrained by the modeled magnetospheric configuration at the time of observation and other ancillary information.

2. Observations

We report in Section 2.1 observations of potassium and sodium in Mercury's exosphere taken at the McMath–Pierce solar telescope on Kitt Peak, Arizona, in support of the first MESSENGER flyby (M1) on January 14, 2008. In Section 2.2, we present observations of magnesium taken with the Ultraviolet and Visible Spectrometer (UVVS) channel of MESSENGER's Mercury Atmospheric and Surface Composition Spectrometer (MASCS) instrument during the spacecraft's second Mercury flyby (M2) on October 6, 2008 (McClintock et al., 2009). Although potassium has been observed previously (Potter and Morgan, 1997; Potter et al., 2002, and references therein), we present a map of the ratio of sodium to potassium in Mercury's exosphere. Physical data pertinent to the observations or data reduction are listed in Table 1. The high Doppler shift of Mercury with respect to the Sun is advantageous for these observations.

Table 1
Mercury ephemerides for observations.

Date	Species	R_{orb} (AU)	$\dot{R}$, heliocentric radial velocity (km s^{-1})	Phase angle (°)	Angular diameter (arcsec)
January 17, 2008	Na, K	0.336	−8.72	63	6.2
October 6, 2008	Mg	0.342	−9.16	173	N/A

2.1. Observations of the sodium and potassium exospheres

Observations of the potassium exosphere of Mercury were obtained at the McMath–Pierce solar telescope on January 17, 2008, three days after the first MESSENGER flyby. We observed the K D_2 line at 766.49 nm at rest in air; the K D_1 line is at 769.8974 nm in air. A large Doppler shift is advantageous for potassium observations in order that the atomic line at rest with respect to the planet should coincide with the continuum region of the solar flux and be removed from the telluric absorption lines as illustrated in Fig. 1. We used a 5″ × 5″ image slicer (where ″ denotes arcsec) to direct the light from a 5″ × 5″ square area on the planet to the entrance slit of the stellar spectrograph at the telescope. Because the angular diameter of Mercury as viewed from Earth was 6.17″, three different observations covering a 5″ × 5″

area were mosaicked together to produce a 5″ × 10″ image covering the entire illuminated planet (Fig. 2). The phase angle of Mercury as seen from Earth was 63°, and we were primarily observing the dawn side.

The K observations were reduced to column abundance using a K D_2 g-value (photons s^{-1} atom^{-1}) of 107.7 computed at a heliocentric radial distance R_{orb} = 0.336 AU and a heliocentric radial velocity, $\dot{R}$ = −8.7 km s^{-1} (16:00 UTC). Note that the solar flux as seen at Mercury is shifted blueward (toward shorter wavelengths), but the emission in the exosphere is on the red side of the solar Fraunhofer feature as seen from Earth. The g-value (photons s^{-1} atom^{-1}) was computed using the solar flux atlas at the Kitt Peak National Observatory (KPNO) McMath–Pierce solar data archives (Kurucz et al., 1984) and an oscillator strength, f-value, of 0.682 for K D_2 from the National Institute of Standards and Technology (NIST) atomic database (Ralchenko et al., 2008). In spite of the large g-value and high solar continuum, the line is still very weak. Pertinent observational data for the K line are listed in Table 2. The heliocentric distance of Mercury, R_{orb}, was obtained from the Jet Propulsion Laboratory (JPL) Horizons website at the mean time of the observations. The photo-ionization lifetime of K listed in Table 2 is from Fulle et al. (2007); that for Na is derived from the theoretical cross section (Huebner et al., 1992), both at
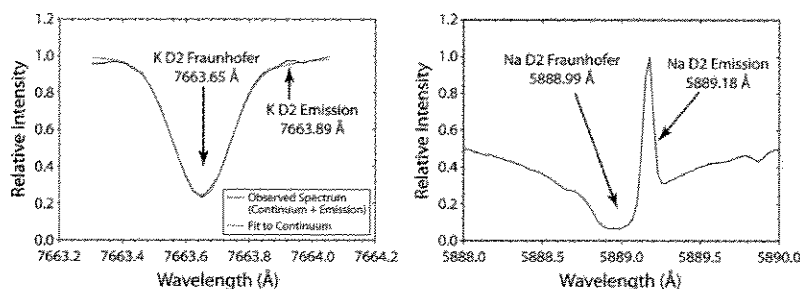

Fig. 1. A (left) The K D_2 emission feature (766.389 nm) is redshifted out of the solar Fraunhofer line at 766.365 nm Doppler-shifted wavelength. Extraction of the line emission was performed for each pixel in the three-dimensional dataset (x, y, λ) by subtraction of the continuum shown by the red line, where x and y are east/west and north/south directions, respectively, and λ is wavelength. Because the K line is weak, the pixels were binned by 2 in each spatial dimension. B (right) The Na D_2 line is similarly redshifted, but the line is strong. Note that the Na Fraunhofer lines are broader than those of the K lines; thus, the Na emission is not shifted completely into the continuum. The continuum under the Na emission was fit with a polynomial to extract the line emission at each pixel. The emission was calibrated using a Hapke model of the surface continuum.
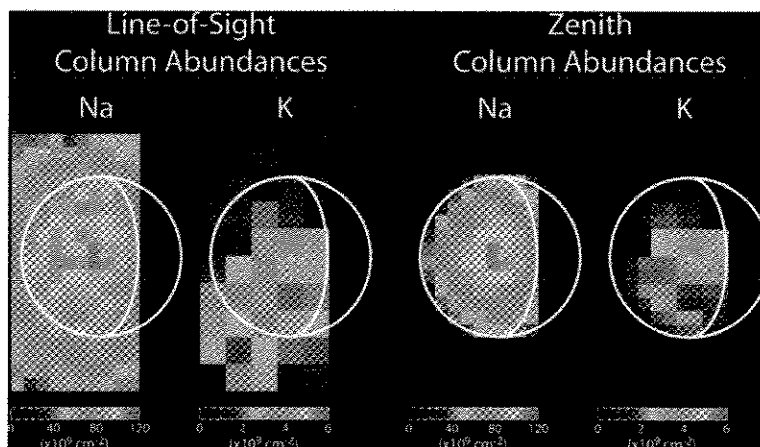

Fig. 2. Potassium and sodium in Mercury's exosphere were observed on the same day, January 17, 2008. These images were made from a mosaic of three overlapping 5″ × 5″ observations obtained with the image slicer placed at the input to the stellar spectrograph at the McMath–Pierce solar telescope on Kitt Peak. The phase angle is 63°. North is at the top, and the terminator is to the right on each image. The line-of-sight column abundance is shown in the left pair of images for Na and K. The zenith column abundances (normal to the surface) are shown in the rightmost pair. The purple pixels in the K image are noise-equivalent column, so K is concentrated near the equator in the northern hemisphere (orange pixels) and at high latitudes in the southern hemisphere (green pixels).

Table 2
Physical data for the potassium and sodium observations.

Parameter	Value
Wavelength (nm), K (D_2) (rest)	766.49
g-value K (D_2)	107.72
K photo-ionization lifetime	5.1×10^3 s (1.4 h)
Wavelength (nm), Na (D_2)	588.995
g-value Na (D_2)	38.2
Na photo-ionization lifetime	1.86×10^4 s (5.2 h)
Sub-solar longitude	182°E
Sub-Earth longitude	120°E
Mean anomaly	301.5°

R_{orb} = 0.336 AU. Because the photo-ionization rates depend on the EUV flux, which depends on the solar cycle, we have used the rates calculated for 'quiet' Sun.

We obtained observations of the sodium D lines with the McMath–Pierce solar telescope using the 5″ × 5″ image slicer on each day during January 12–17, 2008, in support of the first MESSENGER flyby. The Na D_2 line at 588.995 nm (at rest) was observed with the same instrument and identical setup as for potassium except for the wavelength setting. The data reduction process has been described in detail by Killen et al. (2001), and the calibration procedure has been described by Killen et al. (1990). Because the image of Mercury was slightly larger than the field of view of the image slicer, mosaicked images of both sodium and potassium were made to determine the map of Na/K emission above the sunlit disk of Mercury (Fig. 3). Note that the sodium D line emission is much more intense than the potassium D line emission, as illustrated in Fig. 1, primarily because the K abundance is much less than that of Na. Both the background solar flux and the oscillator

strength of the potassium D lines are strong. The signal to noise (S/N) in the Na D_2 emission is 100 for the brightest pixel in the figure. The S/N for the K D_2 emission line is 7 for the brightest pixel. Thus the noise-equivalent column is 10^9 cm^{-2} for Na and 7×10^8 for K. All of our observed column abundances in Na had S/N values between 100 and 10, and our S/N values for K were between 10 and 1.4. The K abundance in the northern hemisphere is very low, especially at high latitudes.

Although the pixels in the K data shown in Fig. 2 were averaged over a 2 × 2 pixel region, the actual observed pixel elements were retained so that the division could be done. Potassium pixels in the fourth and fifth rows from the bottom (south) and columns 1–8 from left (west) were replaced by the averages of rows 2, 3, 6, and 7 in their respective columns (i.e., the adjacent rows). Those pixels appeared to have data dropouts (see Fig. 2) but were off the planet except for the last two and would not contribute to the average Na/K ratio. The line-of-sight Na/K ratio in the southern hemisphere (~36) is close to the smallest ratio found in the datasets considered by Potter et al. (2002), whereas the ratio in the northern hemisphere (~74) is near the mid-value found previously. Note that Potter et al. (2002) published only the average of the pixel ratios, although the ratios were computed in the same way as for Fig. 3A. The large Na/K ratio in the northern hemisphere reflects the fact that most of the K values in the northern hemisphere are noise-equivalent column. If we exclude from the average those pixels for which the K is at noise-equivalent column and ratio the zenith column abundances, the Na/K ratio in the northern hemisphere is 49 and that in the southern hemisphere is 22. There is a small excess of Na in the northern hemisphere relative to the global average value and a large excess of K in the southern hemisphere. The pixels outside of the illuminated disk
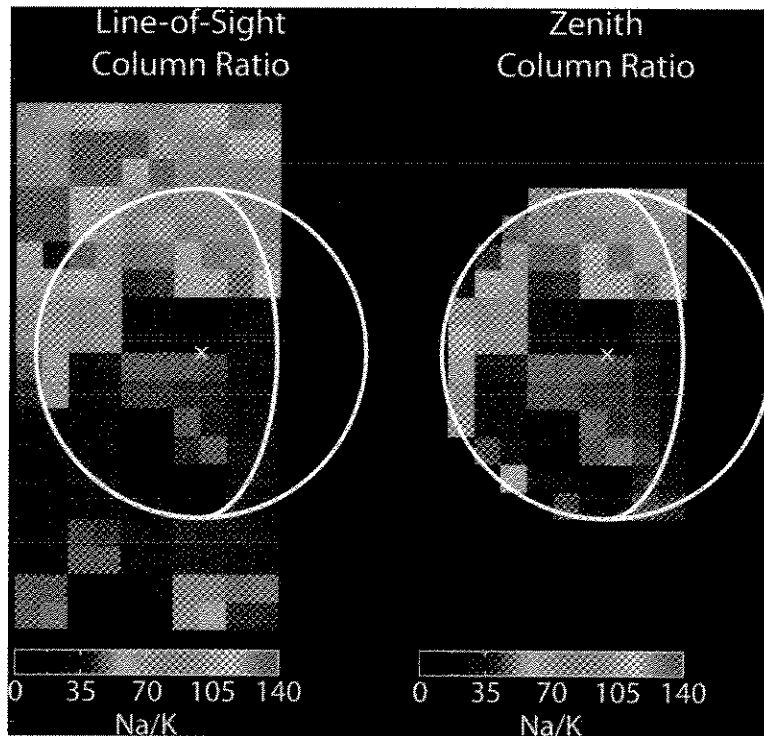

Fig. 3. A (left) Sodium-to-potassium ratio map from line-of-sight column abundances. B (right) Ratio from column abundances reduced to zenith columns. The values of Na/K ratio greater than 70 are dominated by noise in K. Ratios in the southern hemisphere and those near the equator in the northern hemisphere of ~25–35 are obtained with K observations having signal/noise >5. The Na/K in the northern hemisphere computed from the line-of-sight ratios is 74, and that in the southern hemisphere is 36. The sub-Earth point is marked with an x. North is at the top, and the terminator is to the right.

were not counted in the ratios because the K line is weak and noise dominates the ratio off the disk. In addition to noise, the difference in scale heights would affect the ratio off the disk.

Zenith column abundances, the integrated number density normal to the surface, were derived for each pixel from the line-of-sight column abundances at the same pixel using a Chamberlain exosphere and a temperature of 1500 K for both Na and K (Chamberlain and Hunten, 1987, chapter 7), under the assumption of a locally uniform exosphere. The derived average Na zenith column in the north, 4.4×10^{10} cm^{-2}, and that in the south, 3.3×10^{10} cm^{-2}, are within the range previously derived by Potter et al. (2002), taking into account that Potter et al. (2002) published line-of-sight abundances. The average did not include the central row (roughly equatorial) because there was an odd number of rows on the planet disk, but the addition of this row did not change the averages. The average K zenith column in the north is 8×10^8 and that in the south is 13×10^8. The derived average K abundance in the north is very close to the noise-equivalent column (7×10^8), while that in the south is 1.9 times the noise-equivalent column. The average Na abundance in the south divided by the average K abundance in the south is 22, excluding pixels for which K is noise-equivalent column, and this is the same as the average of the Na/K computed per pixel. The average of the ratios of Na/K computed per pixel in the north is dominated by the values near the limb where the K column is the noise-equivalent column unless those pixels are excluded from the average. The Na spatial variation represents only a 10% excess in the north relative to the average value over the entire Earth-facing illuminated disk. The observed K that is above noise level is in the southern hemisphere or close to the equator in the northern hemisphere. This local variation is different from the global variation seen in the datasets analyzed by Potter et al. (2002), who found that K and Na vary similarly (i.e., both north or south). We find that the Na excess is in the northern hemisphere and the K excess is in the southern hemisphere. The Na is more or less peaked at the subsolar point. However, the distribution of K is different. In the northern hemisphere, K is almost entirely confined to within 30° of the equator and near the subsolar point, where the maximum column abundance is about 5.5×10^9 cm^{-2}; whereas in the southern hemisphere, K is most abundant at high latitudes, where the column abundance is about 4×10^9 cm^{-2}. Because the Caloris basin was visible in the northern hemisphere above 25° latitude at the time of the observations and the K was weakest there, we conclude that the Caloris basin was not an enhanced source of K to the exosphere.

2.2. Observations of magnesium

Magnesium was observed in Mercury's exosphere by the MESSENGER MASCS instrument during the second Mercury flyby (M2) by its 285.3-nm emission line (McClintock et al., 2009). MASCS is a scanning grating spectrometer, so that individual emission lines are observed sequentially (McClintock and Lankton, 2007). Herein we analyze observations taken during the "tail-sweep," "fantail," and terminator regions, respectively, as discussed in McClintock et al. (2009). The tail-sweep geometry is illustrated in Fig. 4. Because MASCS observed across the nightside shadow, in the analysis we correct for the fact that, although there is gas in the shadow, it cannot emit there because the emission lines are due to resonant transitions excited by the absorption of solar radiation. This geometry is discussed in Appendix A. The tail-sweep observations were designed to sweep through a vertical distance bounded by ±3 Mercury radii (R_M) as the spacecraft approached Mercury, so the spacecraft rotation angle increased monotonically from ±5° to ±40°. The data analyzed in this paper are confined to ±4° of the equatorial plane in order to avoid issues involving observations at high pointing angles with respect to the
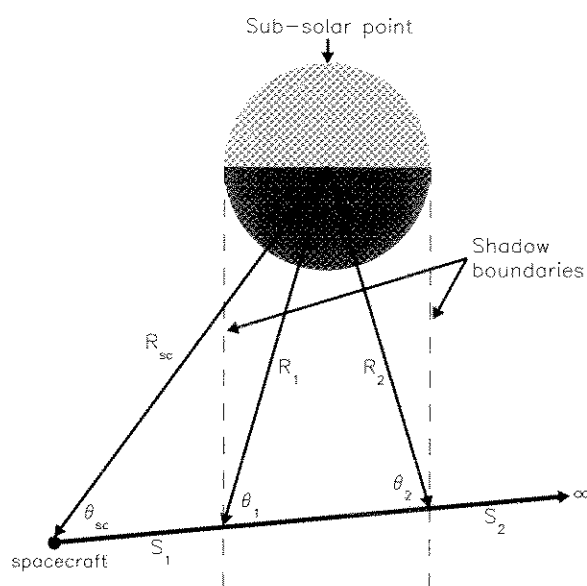

Fig. 4. Shadow geometry for the tail observations used in fitting the parameters for the Chamberlain exosphere. The spacecraft is at the position labeled "spacecraft," and the MASCS instrument looks across the tail at an angle θ_{sc} with respect to the radial vector from the planet center to the spacecraft towards infinity. The dashed lines delineate the shadow boundaries, and the distances R_1 and R_2 are the radial distances from the planet center to the shadow boundary nearest and farthest from the spacecraft, respectively.

equatorial plane. In addition to the angle north/south with respect to the equatorial plane, we took into account the look angle with respect to the y-axis, which is in the equatorial plane perpendicular to the Sun–Mercury line, positive dawnward. These angles vary throughout the observational sequence. Observations in the tail region are illustrated in Fig. 5A, smoothed via interpolation between observed points using standard Interactive Data Language (IDL) routines. Because of the smoothing, the image in Fig. 5A should not be used in a quantitative analysis but gives visual clues only. The physical data used in the data extraction and model are given in Table 3. The noise-equivalent column is 6×10^7 Mg atoms cm^{-2} from the surface to 16,000 km behind the planet, and 4×10^7 from 16,000 km to 40,000 km behind the planet, so S/N is ~10 in this region. The solar spectrum is shifted blueward due to Mercury's motion toward the Sun, but the flux absorbed by an atom at rest with respect to the planet is on the red wing of the solar line. The g-value in Table 3 reflects this frequency shift (Killen et al., 2009).

A least-squares fit to the data was run on a series of Chamberlain exosphere models solved at each observation point for the second Mercury flyby observational geometry for a series of 10 values of surface density (n_0) and 10 values of temperature to determine the minimum variance solution (see Appendix A). The tangent column observed by MASCS within 4° of the equatorial plane was fit to a Chamberlain exosphere (Chamberlain and Hunten, 1987) at the observed angles with respect to the planetary normal, taking the shadow into account. We also included a possible dawn–dusk asymmetry multiplicative factor in the solution to account for a possible dawn–dusk asymmetry, but for magnesium this factor converged to unity. The full Chamberlain exosphere model was used in this analysis, even in the tail region, and is appropriate because, unlike sodium, Mg is not subject to radiation pressure and has a very long lifetime against photo-ionization, 57.5 h (Table 3). The best solution for n_0 and T is given where the least squares deviation from the solution for all data points is minimum. The magnesium data taken in the M2 tail sequence (Fig. 5B, asterisks)
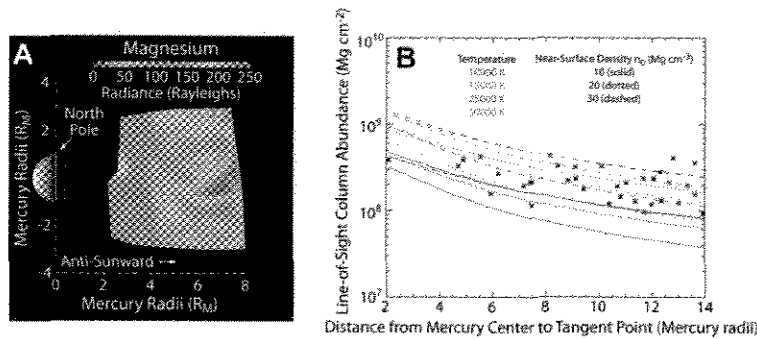
Fig. 5. (A) Observations of the magnesium tail of Mercury taken during the second MESSENGER flyby (McClintock et al., 2009). The MASCS instrument is a scanning grating spectrometer, so that different emission lines are observed sequentially. The pattern observed in the image is merely the result of smoothing via interpolation between observed points using standard IDL routines. The actual observed emission is peaked in the equatorial plane, but because the observations were taken through the anti-sunward shadow, the observed emission includes only the illuminated portion of the exosphere outside the shadow. (B) A least-squares solution was fit to a matrix of Chamberlain exospheres of different temperatures and near-surface densities. The models are for integrated emission across the tail, taking into account the lack of emission in the shadow. The best fit to the data, shown by asterisks, was for a temperature of 50,000 K and a density, n_0, of 16 cm^{-3}; however, this fit is probably influenced by the single observation at a radial distance 2 R_M behind the planet. We allowed for the possibility of a different density on the dawn and dusk sides, but the solution converged to the same number density, giving no dawn/dusk asymmetry. A number of models are shown for temperatures of 10,000, 15,000, 25,000 and 50,000 K, respectively, each for surface number densities of 10, 20, and 30 Mg atoms cm^{-3}. Note that we are seeing only the escaping component of the exosphere in this region. The models are such that a higher surface number density will compensate for a lower temperature source, but lower temperature solutions require higher emission near the planet than observed. More data points in this region would give greater confidence in the solution.

Table 3
Physical data for Mg.

Parameter	Value
g-value at M2 for 285.296 nm line (vacuum)	0.3177 photons s^{-1} atom^{-1}
Photo-ionization rate at Earth	5.66 × 10^{-7} s^{-1}
Photo-ionization rate at Mercury, M2	4.827 × 10^{-6} s^{-1}
Ionization lifetime at Mercury, M2	57.5 h

converged to a Chamberlain exosphere with a near-surface density $n_0 = 16$ cm^{-3} and a temperature of 50,000 K (Fig. 5B). However, the solution is by no means unique as shown by the curves in Fig. 5B for solutions with temperatures ranging from 10,000 K to 50,000 K and surface number densities of 10, 20 and 30 cm^{-3}, respectively. A low temperature can be compensated by a high density at the surface to fit the data in the tail region. The best-fit solution is forced by the single low data point at 2 R_M. The presence of an extended Mg exosphere cannot be due to radiation pressure, and loss by photo-ionization is negligible.

We performed the same type of solution on the Mg "fantail" data obtained as the spacecraft rolled through 180° from boresight pointing dawnward, through north, toward a duskward line of sight as the spacecraft moved toward the planet from approximately 2550 km to approximately 350 km behind the planet (Fig. 6B). This geometry was taken into account in the analysis. The Mg fantail data are illustrated by the asterisks in Fig. 6B, along with the least-squares solution shown by the solid red line, and models at temperatures of 25,000, 40,000, and 50,000 K, respectively, at surface densities, n_0, of 5 and 9 cm^{-3}. The lower set of lines are those run at $n_0 = 5$ cm^{-3}, and the upper set of curves are those run at $n_0 = 9$ cm^{-3}.

The solution for the fantail converges to a lower temperature, 25,000 K, and a lower surface density, 9, than the solution for the tail data, but the temperature is poorly constrained in either case. However, the temperature derived from the fantail data is still 20 times higher than that indicative of a photon-stimulated desorption (PSD) source, which would give 1200 K (Madey et al., 1998), and 5 times higher than that expected from a hypervelocity impact source, which would give about 5000 K or less (e.g., Berezhnoy and
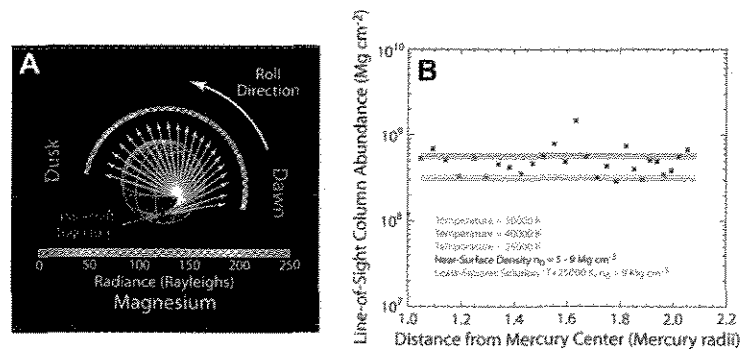

Fig. 6. (A) Observations in the "fantail" were taken during the spacecraft roll beginning with the line of sight (LOS) toward dawn and ending with the LOS toward dusk as the LOS swept through north. There is a slight increase in emission to the northwest (dusk side), but the line of sight was closer to the planet on that side. (B) Fantail data illustrated by the asterisks are plotted with a least-squares solution (red), at a temperature of 25,000 K and surface number density of 9 cm^{-3}. Other models are shown for temperatures of 25,000, 40,000, and 50,000 K with surface number densities of 5 cm^{-3} (lower set of lines) and 9 cm^{-3} (upper set of lines). The plotted column abundances are observed line-of-sight abundances. This geometry does not constrain temperature as a result of the fact that the observations are in the near-tail region at a very limited range of distances from the planet.

Klumov, 2008). The extreme temperature fit in the tail and fantail region is inconsistent with a PSD source for the Mg atoms reaching this region of the exosphere and probably requires a secondary process such as dissociation of a molecular source that was initially vaporized or sputtered from the surface, because the atoms are more energetic than they would be if derived from PSD, impact vaporization, or ion sputtering. This inference is consistent with that made from observations of Ca (Killen et al., 2005).

After the spacecraft completed the roll maneuver, MASCS executed Mg observations in the near-terminator region while still on the nightside (McClintock et al., 2009, Fig. 2). For this dataset the boresight was looking at the nightside surface, but only that portion of the exosphere above the shadow was illuminated and therefore seen in emission. We modeled the emission between the spacecraft and shadow, taking into account the boresight angles with respect to the surface. A fit to the Mg data in the near-terminator region (Fig. 7B) was less successful than the fits to the tail and fantail data, probably because the exosphere is non-uniform in this region and the data cannot be made to fit a single model. In the terminator region the observed line-of-sight column, that between the spacecraft and the shadow, sampled a restricted range of the exosphere. Each data point (asterisks) represents not only a different spacecraft distance but also a different distance behind the terminator. Fits are shown for a temperature of 70,000 K (green) and a temperature of 10,000 K (red) with surface number densities of 50 (lower curves) and 100 cm^{-3} (upper curves). As the spacecraft approached the terminator, the data were fit by a progressively lower temperature and a higher surface number density. The data can be fit with a temperature of 10,000 K provided that the surface number density is above 50 cm^{-3}, but the fits are non-unique. The first three points were not included in the fit because they represent a very short line of sight in sunlight.

3. Data analysis

3.1. Surface composition

The surface composition of Mercury is not known at present. Table 4 shows abundance of elements from lunar soils that will be used to constrain possible surface compositions at Mercury: Luna 16 and 24, Apollo 11 low K and high K, and Apollo 17 orange glass (Heiken et al., 1991). In the following discussion, we consider the implications for exosphere models of a Mg abundance in the regolith of 5% by number (consistent with the mean of the Apollo 11 and Luna measurements) and 8.6% by number, consistent with Apollo 17 orange glass.

3.2. Sodium and potassium

The potassium map obtained on January 17, 2008, at the McMath–Pierce solar telescope had 78 pixels in the illuminated portion of the planet. Zenith column abundances, along the normal to the planet surface, were calculated from observed line-of-sight abundances for a Chamberlain exosphere. Although this is not an exact model, it does remove the line-of-sight effects given the assumption of a locally uniform exosphere. The average zenith column abundance of Na in the northern hemisphere was 4.4×10^{10}, and that in the southern hemisphere was 3.3×10^{10}; the average zenith K abundance in the northern hemisphere is 7.5×10^{8}, whereas that in the southern hemisphere is 1.3×10^{9} cm^{-2}. Since the noise-equivalent column for K is about 7×10^{8}, most of the K measurements in the northern hemisphere are consistent with noise, so only an upper limit is determined except for an area near the equator. From the zenith column abundance ratios per pixel, the average Na/K ratio in the north, excluding pixels for which K
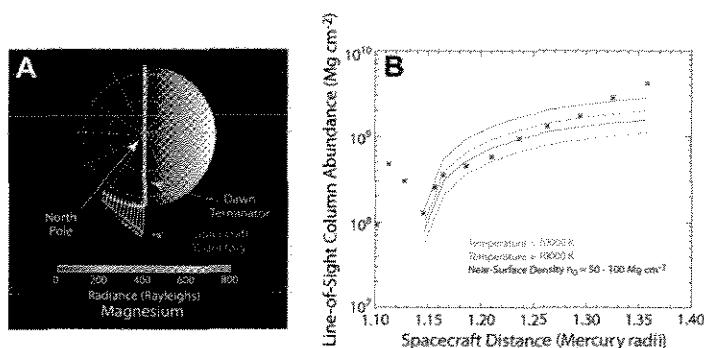

Fig. 7. (A) Illustration of the geometry of the near-dawn terminator observation. The arrows show the direction of the UVVS line of sight during each observation, and the color represents the observed intensity. The observations were approximately in the equatorial plane. (B) Models fit to the near-terminator data indicate a best-fit solution at a temperature of 35,000 K and density n_0 of 75 cm^{-3}; however, we show models at temperatures of 10,000 K and 70,000 K, respectively, each at surface number density of 50 and 100 cm^{-3}. Each individual data point (∗) is obtained at a different distance behind the terminator, with those at a larger spacecraft distance from the planet closer to the terminator. As the spacecraft moves toward the dawn terminator a longer path length is observed, and the path intersects less shadow. The noise-equivalent column is 6×10^{7} cm^{-2} from the surface to 16,000 km behind the planet, thus S/N is ~1.7 for the least emission. Points below 1.15 R_M were not modeled because the path length in sunlight was too small. The best-fit temperature decreases and the best-fit surface number density increases as the spacecraft approaches the terminator (dawn). There does not appear to be a single solution in this region. A simple Chamberlain exosphere with $n_0 = 75$ cm^{-3} and a scale height of ~3100 km (corresponding to 35,000 K) would have a column abundance of 2.3×10^{10} atoms cm^{-2}.

Table 4
Model abundance of elements for Mercury surface materials and abundances in selected lunar soils.

Species	Model 1 #% (wt.%)	Luna 16 #%	Luna 24 #%	Apollo 11 high K #%	Apollo 11 low K #%	Apollo 17 orange glass #%
Ca	2.15 (1.3)	4.9	4.7	4.4	4.44	3.1
Mg	5–8.6	5.3	5.9	4.2	4.0	8.6
Na	0.34 (0.35)	0.27	0.22	0.39	0.31	0.28
K	0.03 (0.02)	0.06		0.18	0.03	0.045

is at noise-equivalent column, is 48.5. The average Na/K ratio in the south, also excluding pixels for which K is noise-equivalent column, is 22 where the S/N in K is 5–10.

Note that historical data records give the ratios of line-of-sight column abundances. To facilitate comparisons, we compute these ratios as well even though they have line-of-sight effects. The line-of-sight average Na abundance was 9.9×10^{10} in the northern hemisphere and 8.2×10^{10} in the southern hemisphere. The average K line-of-sight abundance in the northern hemisphere was 1.8×10^{9}, and that in the southern hemisphere was 2.6×10^{9} cm^{-2}. The average line of sight values are roughly twice those of zenith column values. The very large Na/K ratio in the northern hemisphere reflects the fact that the K abundance is very low in the northern hemisphere at this time. More interesting is the spatial distribution of K. In the northern hemisphere K is almost entirely confined to within 30° of the equator, whereas in the southern hemisphere K is mostly south of 30°S.

Berezhnoy and Klumov (2008) concluded that for an impact-vaporization source of the exosphere of Mercury, the ratio of Na atoms to all Na in the exosphere (atomic and molecular) is 0.7, whereas the ratio of K atoms to all K is 0.4. If we assume that these ratios hold for all source processes, and the average ratio is most representative of source processes, then the Na/K ratio in the exosphere can be approximated as

$$\frac{Na_{gas}}{K_{gas}} = \frac{Na_{surf}}{K_{surf}} \frac{\tau_{ioniz}(Na)}{\tau_{ioniz}(K)} \frac{Na_{gas}}{Na_{total}} \frac{K_{total}}{K_{gas}} \qquad (1)$$

where Na_{gas}/K_{gas} is the measured exospheric ratio (37), Na_{gas}/Na_{total} = 0.7, and K_{gas}/K_{total} = 0.4 from Berezhnoy and Klumov (2008). Given photo-ionization lifetime of Na from Huebner et al. (1992) and that for K from Fulle et al. (2007) (Table 2), we derive the ratio of abundances in the regolith, Na_{surf}/K_{surf}:

$$37 = Na_{surf}/K_{surf}(3.75 \cdot 1.75) \qquad (2)$$

This last expression yields a ratio of Na/K in the soil of approximately 5.6. For the ratio of Na/K found in the southern hemisphere, where the K abundance is above the noise-equivalent column, the observed atmospheric Na/K ratio is 22, yielding a Na/K ratio in the surface of 3.4. The K content of Apollo 17 pristine orange glass is 0.045% by number (625 μg/g). The Na/K ratio in Apollo 17 pristine orange glass is 6.2, and that in Luna 16 soil is 4.5. The average of our derived ratios of Na/K in the soil is 4.5 and is therefore consistent with the abundance ratio in Luna 16 soil, for which the K abundance is higher than that in Apollo 17 orange glass but lower than that for high-K Apollo 11 lunar samples. The Na/K ratio derived from the northern hemisphere is consistent with Apollo 17 orange glass, a pyroclastic glassy deposit.

Photon-stimulated desorption has been shown to be an important, if not dominant, source of alkalis in the lunar and mercurian exospheres (e.g., Madey et al., 1998; Madey and Yakshinskiy, 1997; Yakshinskiy and Madey, 1999, 2004, 2005). Potter and Morgan

(1997) showed that the variations of Na and K in Mercury's exosphere are correlated and depend on the flux of solar ultraviolet (UV) radiation. Their ratios of Na/K in the timeframe December 6–10, 1990, varied from 130 to 260; these are much higher than found here but probably included line-of-sight effects and also may indicate that low values of K abundance in the exosphere are consistent with noise-equivalent column. Potter et al. (2002) found an average Na/K ratio in Mercury's exosphere of about 100. There were three dates reported in that paper on which the Na/K ratio was most similar to the one found here: January 11, 1998 (67.7), April 26, 1999 (66.3), and May 2, 1999 (69.5). We have included the observations of Potter et al. (2002) and our observations in Table 5 along with orbital distance from the Sun, true anomaly angle, heliocentric radial velocity, g-value of Na(D$_1$ + D$_2$), Na/K, radiation acceleration (cm s^{-2}), and F10.7. The F10.7 index is derived from the 10.7-cm radio flux, which has been shown to be correlated to the solar Lyman α flux and is a standard proxy for solar ultraviolet (UV) flux. The average value of F10.7/(Na/K) is 14.5, regardless of whether F10.7 is high or low. The values of Na/K ratio vs. Lyman α flux normalized to the heliocentric radial distance (Fig. 8) give a correlation coefficient of 0.66, which implies a weak relationship between UV radiation and the Na/K ratio in the exosphere (Fig. 8). The values of Lyman α flux (photons cm^{-2} s^{-1}) in Table 5 are from the Laboratory for Atmospheric and Space Physics (LASP) Interactive Solar IRradiance Datacenter (LISIRD) website (http://lasp.colorado.edu/LISIRD/) (Snow et al., 2005) and have been rotated to the orbital position of Mercury for a solar rotation rate of 27 days (disk average) and the phase angle given in Table 5. We conclude that the solar UV flux provides an important source of alkalis to the exosphere but cannot be the only source. The dependence on UV flux for the Na/K ratio implies that Na and K vary differently with UV flux.

3.3. Magnesium

3.3.1. Impact vaporization at the time of M2

The magnesium observations reported here were obtained during the second MESSENGER flyby on October 6, 2008. Mercury's orbital distance was 0.342 AU. We estimated the impact vaporization rate on this date using the planar impact approximation method (Melosh, 1989, chapter 4; Morgan and Killen, 1998; Killen and Sarantos, 2004), and we scaled the impact flux from Earth orbit measured by Love and Brownlee (1993) to Mercury orbit following the mathematical formulation in Cintala (1992). We approximated the thermodynamic properties of the meteoroid impactors and the regolith using the "regolith" constants in Cintala (1992) and the impact parameters for Al onto enstatite given in Melosh (1989), Appendix B. Using this formulation the total vaporization rate at R_{orb} = 0.342 AU is 2.7×10^{7} cm^{-2} s^{-1} for impact of aluminum (a proxy for asteroid composition) onto regolith, and the Mg

Table 5
Observations of Na/K and relevant physical parameters.

Date	R_{orb} (AU)	TA (°)	Phase (°)	$\dot{R}$ (km s^{-1})	Phase (°)	Na/K	Radiation acceleration (Na)	F10.7	$\frac{F10.7}{Na/K}$	Ly α × 10^{11}	Ly α/R^2 × 10^{11}
December 6, 1990	0.365	274.5	77	−10.0	57.9	214	169.2	2277	10.6	5.74	43.1
December 7, 1990	0.359	279.5	80	−9.94	59.5	155	174.0	2288	14.8	5.78	44.8
December 8, 1990	0.353	284.2	84	−9.76	60.7	260	177.6	2304	8.9	5.81	46.6
December 9, 1990	0.348	289.1	88	−9.5	61.7	157	180.2	2374	15.1	5.82	48.1
December 10, 1990	0.342	294.1	93	−9.2	62.1	130	181.3	2407	18.5	5.82	49.8
January 11, 1998	0.424	129.5	62	+7.8	34.2	67.7	99.9	1017	15.0	3.91	21.7
April 26, 1999	0.444	216.5	77	−6.0	22.1	66.3	64.5	1058	15.9	4.18	21.2
May 2, 1999	0.419	235.5	66	−8.3	37.9	69.5	110.7	1379	19.8	4.45	25.3
January 17, 2008	0.334	300.2	63	−8.7	61.6	60.	180.0	737	12.2	3.62	32.4

Notes: R_{orb} = orbital distance in AU. TA = true anomaly angle. $\dot{R}$ = heliocentric radial velocity (km s^{-1}).
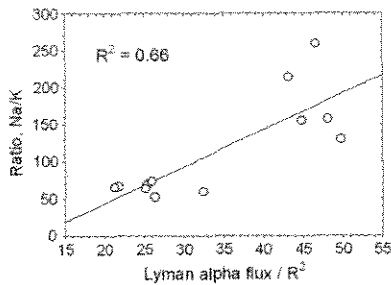
Fig. 8. The Na/K ratios from Potter et al. (2002) are plotted vs. Lyman α/R_{orb}^2 along with that from this paper (data point at Ly $\alpha/R_{orb}^2 \approx 32$). The Na/K ratio is moderately correlated with the Lyman α radiation. We plot the average Na/K ratio over the illuminated disk to avoid complications regarding scale-height effects off the disk and added noise caused by low-signal K observations as the K decreases away from the planet. Although a linear correlation coefficient of 0.66 does not represent a strong correlation, it indicates that 66% of the variation can be explained by a linear correlation between the ratio of Na/K and Lyman α flux. However, our data point is much lower than those found earlier because we rejected K values that have $S/N < 1$. This indicates that although UV radiation is involved, other factors are effective in the ejection and loss processes.

vaporization rate is 2.3×10^6 atoms cm^{-2} s^{-1} for an 8.6% surface abundance of Mg or 1.3×10^6 cm^{-2} s^{-1} for a 5% abundance of Mg.

In addition to the Cintala (1992) and Morgan and Killen (1998) analyses of meteoroid impact rates onto the surface of Mercury, several new estimates have been published. Notably, Borin et al. (2009) have estimated a meteoroid impact flux onto Mercury 170 times the Cintala rate. This of course has important implications concerning the exosphere. Killen et al. (2001) used the Cintala (1992) mathematical formulation for transfer of material from Earth orbit to Mercury orbit with the Love and Brownlee (1993) interplanetary dust particle (IDP) flux rates and the Morgan and Killen (1998) impact vaporization code to estimate the magnitude of various contributions to the sodium exosphere and obtained an estimate of 20–30% of the sodium exosphere contributed by impact vaporization. Thus, an increase of the Love and Brownlee (1993) flux by a factor of only 3–5 would supply the entire exosphere. Morgan et al. (1988) estimated that meteoroids supply up to 1.4×10^{24} Na atoms s^{-1} to the exosphere, or a factor of about 5 greater than the Cintala rate, and concluded that meteoroid vaporization can supply the full Na exosphere of Mercury. The main reason for the larger rate given by Morgan et al. (1988) is the use of a velocity distribution function from Southworth and Sekinina (1973). An impact flux 170 times the Cintala rate would either overwhelm the exosphere, or we would have to conclude that impact vaporization is either less efficient than previously estimated, that impact vapor quickly condenses, leaving only 2% of the vapor in the exosphere, or that the vaporization products are not fully measured, possibly being in molecular form. The distribution of various elements in the exosphere appears to be inconsistent with uniform impact vaporization by micrometeoroids (e.g., Burger et al., 2010), mainly because of high-latitude enhancements, a dawn enhancement in Ca, and rapid variability.

The Mg observations in Mercury's tail region were fit by a 15,000–50,000-K gas, which is much hotter than would be expected from direct impact vaporization. Although the temperature is not well constrained, and indeed the velocity distribution is likely to be non-thermal, it is clear that a hot vapor is required to fit the data. Very hot (30,000 K) Ca atoms have been observed in Mercury's exosphere from ground-based observations (Bida et al., 2000; Killen et al., 2005) and were attributed to vaporization of calcium in molecular form with subsequent dissociation, which imparts additional energy to the atomic fragments. We suggest that

the same process produces the hot Mg that we have observed in the tail region. The dissociation energy of MgO is 3.35 eV (Murthy and Bagare, 1978). If dissociated by a Lyman α photon (10.2 eV) the products would have an excess energy of 6.8 eV between them. If each fragment has 3.4 eV, then the equivalent temperature is 40,000 K. If the gas temperature is 40,000 K, the mean velocity of the gas is 5.2 km s^{-1}, which is above escape velocity (4.2 km s^{-1}). Thus those Mg atoms that are derived from dissociation of MgO will escape. Their lifetimes will be the photo-ionization lifetime (Table 6). The Mg ionization rate is 5.66×10^{-7} s^{-1} at Earth (quiet Sun) or 4.84×10^{-6} s^{-1} at Mercury during the second MESSENGER flyby. Thus the Mg photo-ionization lifetime was 2.0×10^5 s, or 57 h. At a velocity of 5.8 km s^{-1}, a Mg atom would travel 475 planetary radii on average before becoming ionized. The Hill sphere, where the gravitational field of the Sun dominates over that of Mercury, is at $\sim 81~R_M$. Therefore ionization is not a major loss process for Mg in the region that we observe. Note that even though the Mg atoms in the tail have very high velocities relative to the planet, the g-values, and hence the derived column abundances, only differ by 5% between that for a Mg atom at rest with respect to Mercury (g-value = 0.317) and one traveling at 5 km s^{-1} anti-sunward (g-value = 0.300). Therefore the assumed g-values do not introduce a large error in the derived column abundances even if the assumed velocities are incorrect.

The fraction of Mg(atoms)/Mg(total) from impact vaporization at quenching was estimated by Berezhnoy and Klumov (2008) to be less than that of the alkali species. At 4000 K, the equilibrium fraction of Mg to MgO is about 2 (Berezhnoy and Klumov, 2008). We assume that half of the Mg + MgO will condense, leaving a gas release rate of $0.7 \times 10^6 < dn/dt < 1.2 \times 10^6$ for Mg abundances of 5% and 8.6%, respectively. If we assume that 30% of the impact-derived Mg is in the form of MgO, then the very hot portion of the Mg exosphere should have an impact vapor source rate of $0.3 \cdot 1.2 \times 10^6$ cm^{-2} s$^{-1} \approx 3.6 \times 10^5$ cm^{-2} s^{-1} for an 8.6% Mg abundance in the regolith or 2×10^5 cm^{-2} s^{-1} for a 5% abundance, using the vapor code described in Morgan and Killen (1998). The observed column is estimated to be 7×10^9 cm^{-2} normal to the surface. If the exosphere is that portion from the surface to the Hill sphere (81 planetary radii) and the Mg atoms have a mean velocity of 5 km s^{-1}, then the lifetime of the Mg atom in the exosphere is 4×10^4 s. Then if the production rate of Mg is 6.75×10^5 s^{-1}, and the lifetime is 4×10^4 s, we would expect to see a column of 2.7×10^{10} Mg atoms. Given that we see 26% of that, we conclude that this is the fraction of the vapor initially in the form of MgO that was dissociated to produce the very hot atomic Mg observed. This inference is consistent with the result from Berezhnoy and Klumov, namely that 30% of the vapor is in the form of MgO. We conclude that impact vaporization of Mg-bearing minerals can produce the observed Mg tail given an abundance of Mg in the regolith of 5–8.6%, if roughly half of the vapor condenses and 30% of the vapor is in the form of MgO as estimated by Berezhnoy and Klumov (2008). This relies on the assumption that the observable lifetime of Mg is the lifetime of the atom to the Hill sphere.

Table 6
Ionization rates for the observed species.

Species	Ionization rate, s^{-1} (at 1 AU; quiet Sun[a])	Ionization rate, s^{-1} (at 1 AU; active Sun[a])	Lifetime at 0.342 AU (s) (quiet Sun[a])
Na	5.99×10^{-6}	6.52×10^{-6}	1.95×10^4
Mg	5.66×10^{-7}	1.08×10^{-6}	2.07×10^5
Ca	7.0×10^{-5}	7.8×10^{-5}	1.67×10^3
K	2.2×10^{-5}	2.4×10^{-5}	5.3×10^3

[a] Ionization rates depend on the solar extreme UV flux, which depends on the solar cycle.

3.3.2. Ion sputtering at the time of M2

Sputter yields of Mg from MgO by low-energy He and Ar ion beams were measured as a function of ion energy by Hine et al. (2007) and fit to the following equations:

$$Y_{He} = a\left(\sqrt{E/E_0} - 1\right) \tag{3}$$

where Y_{He} is the MgO sputter yield from incoming He ions, $a = 0.191$, and $E_0 = 241$ eV;

$$Y_{Ar} = a\left(1 - \sqrt{E_0/E}\right)^{5/2}\left(1 + b\left(\sqrt{E/E_0 - 1}\right)\right) \tag{4}$$

where Y_{Ar} is the sputter yield of MgO by impacting Ar ions, $a = 0.0644$, $b = 7.61$, and $E_0 = 36.5$ eV. These measurements were made for $E < 460$ eV; however, we will employ the equation to estimate yields by solar wind ions. The sputter yield of Mg by 3.3-keV He ions in the solar wind would therefore be about 0.5/ion.

Ignoring for the moment highly charged ions, which normally comprise less than 1% of the solar wind, and assuming that He ions are 4% of the solar wind, the solar wind yield would be

$$\frac{d(Mg)}{dt} = 0.02 f_{sw} f_{Mg} \tag{5}$$

where f_{sw} is the solar wind flux onto the surface of Mercury and f_{Mg} is the number fraction of Mg in the soil. We estimate that the solar wind flux onto the surface of Mercury during the second flyby was 10^{25} ions s^{-1} (e.g., Benna et al., 2010), although this may be an optimistic estimate (e.g., Sarantos et al., 2007). If we assume that the fraction of Mg in Mercury's regolith is 8%, then the sputter yield is about 1.6×10^{22} atoms s^{-1} or a planet-wide average of 2×10^4 Mg cm^{-2} s^{-1}. If the lifetime of the Mg atom to the Hill sphere is 4×10^4 s, the column from sputtering would be about 8×10^8 Mg cm^{-2}, or about 10% of the observed column. Although the sputter yield averaged over the planetary surface is two orders of magnitude less than the estimated hypervelocity impact yield, the local yield in areas of open fields may be comparable, especially at times of enhanced solar wind flux. The local proton flux to the surface can be as high at 10^{11} ions cm^{-2} s^{-1} and averages 10^8 in the open areas (Benna et al., 2010). With a yield per ion of 0.02 f_{Mg} or ~0.002 f_{sw}, the local sputtered Mg rate averages about 2×10^5 cm^{-2} s^{-1} in the cusp regions during the first MESSENGER flyby when the magnetosphere was quiet and the interplanetary magnetic field (IMF) was northward, impeding solar wind access to the surface. The sputter yield may be as high as 0.2/ion, in which case the sputtered Mg rate would be about $(1-2) \times 10^6$ cm^{-2} s^{-1} in the cusp regions during the first MESSENGER flyby. This local rate would be comparable to the impact vaporization rate and would produce hot atomic Mg. If this ion-sputter yield adds to the impact vaporization yield, then the local yield could produce local enhancements equal to 10 times the observed average column, as observed by MESSENGER during the third flyby (McClintock et al., 2009). The estimated sputtering source is therefore a small fraction of the total Mg exosphere but could be important for populating the tail region.

Because the disturbed solar wind can be comprised of enhanced fractions of heavy elements, for instance up to 30% He ions (Wang, 2008), sputtering by highly charged heavy ions may play an important role at Mercury (Kallio et al., 2008). Sputter yields by highly charged ions are known to be significantly enhanced over those by singly charged ions, especially in insulators. This effect is known as "potential sputtering" and has been extensively discussed in the literature (e.g., Kallio et al., 2008). Although the charge-state effect is not as great in highly ionic oxides such as MgO, there is still a significant charge-state effect (Hayderer et al., 2001). If we can correlate enhanced ion sputtering with solar energetic particle (SEP) events at Mercury, we may be able to determine whether the highly charged ions are an important source of sputtered atoms.

Additional laboratory work on sputter yields by highly charged ions is needed to more fully understand this process.

3.3.3. Estimate of photon-stimulated desorption of Mg

Magnesium can be desorbed from MgO by 265-nm laser pulses (Joly, 2002), and PSD yields of Mg from MgO are comparable to those for Na. Although MgO comprises about 15–26% of pyroxene, and the pyroxene abundance is about 40–60% for mare basalts on the Moon, the Mg is present as a silicate. Therefore the PSD yields for Mg from Mercury's surface minerals is highly uncertain at the present. Mg would be desorbed by PSD only if a significant amount of MgO were re-deposited on the surface as a result of impact vaporization.

4. Discussion

Potter et al. (2002) found that the ratio of sodium to potassium in the exosphere of Mercury was highly variable and averaged 100 ± 20, much larger than values observed elsewhere in the Solar System (Table 7). The Na/K ratio in the lunar exosphere is close to that in the lunar crust. We will argue that the Na/K ratio in Mercury's exosphere is in fact much larger than that ratio in the regolith, and that very large ratios of Na/K in Mercury's exosphere may be due to very low abundances of K in the exosphere, where measurements are dominated by noise.

The Na/K ratio in the exosphere of the Moon is in the range 4.4–6, not far from overall average ratio of Na/K in the surface lunar rocks, which is in the range 7–9. Potter et al. (2002) found that radiation acceleration losses were not sufficiently different for sodium and potassium to explain the Na/K high ratio. They proposed that the photo-ionization loss and recycling rates were sufficiently different for sodium and potassium to account for the high ratio. The higher mass of the potassium atom relative to sodium (39 vs. 23) results in a smaller scale height and a larger gyroradius for potassium relative to sodium, which may result in more rapid net loss of potassium from the planet. However, Sarantos (2005) considered relative loss rates of Na and K photoions to the solar wind and concluded that the difference was too small to explain the variations in the Na/K ratio in the exosphere. Our results show that the Na/K ratio in Mercury's exosphere is in the range 22–49, where the ratios are taken only where the observations are above the noise-equivalent column.

A possible explanation for the large variation in the published Na/K ratios at Mercury is the use of improper g-values. This is certainly the case for the high value of Na/K reported in the Earth's atmosphere (Gault and Rundle, 1969). Although the g-values were scaled for the radial velocity of Mercury at the time of the observation, there are two effects that were not taken into account. First, the radial velocity not only affects the continuum at the rest frequency of the atom in the atmosphere of Mercury, but it affects the multiplet structure, since each transition is independently af-

Table 7
Sodium to potassium ratios by number in the Solar System.

Object	Na/K	Source
Mercury exosphere	40–250	Potter et al. (2002)
Io exosphere	10	Brown (2001)
Europa exosphere	25	Brown (2001)
Moon exosphere	6	Potter and Morgan (1988)
Lunar crust	7–9	Lodders et al. (1998, p. 177)
Meteorites	7–14	Lodders et al. (1998, p. 311)
Earth atmosphere	20–150	Gault and Rundle (1969)
Earth seawater	27	Lodders et al. (1998, p. 164)
Earth crust	2	Lodders et al. (1998, p. 143)
Solar System[a]	15	Lodders et al. (1998, p. 80)

[a] Derived from solar spectroscopic and meteoritic (Cl-chondrite) analyses.

fected by the structure of the solar spectrum. Secondly, the velocity of the atom inside the atmosphere was not taken into account in the data reduction. The radial velocity of the bulk atmosphere may vary with the solar zenith angle and the viewing geometry. Third, the K emission is weak and the uncertainty in the abundance is large. Nevertheless there are valid explanations for a variable Na/ K ratio in the exosphere of Mercury. The questions here are why is the source rate variable and why is it different for Na and for K.

There is a moderate correlation between Na/K and Lyman α flux, with a correlation coefficient of 0.6. The measured ratio is either large (on the order of 150–250) for Lyman α greater than 5×10^{11} photons cm^{-2} s^{-1} or small (on the order of <60) for Lyman α less than 5×10^{11} photons cm^{-2} s^{-1}. One explanation is that the rates of supply of volatiles to the extreme surface, or the upper-most few monolayers, and thus to the exosphere, are diffusion-limited, and the diffusion rate for K is less than the diffusion rate for Na (Killen and Sarantos, 2004). Diffusion of atoms from the interior of grains to the extreme surface, or the topmost few monolayers, is required in order to repopulate the layers from which PSD and ion sputtering can eject atoms (Killen and Sarantos, 2004). Diffusion-limited supply is a well-known phenomenon in sputtering (e.g., Roth, 1983). The rate at which Na and K diffuse to the surface of grains of sizes 1 μm to 1 m, at temperatures found on the surface of Mercury, was calculated by Killen and Sarantos (2004) using dif-fusion data from Nyquist et al. (1979). Note that this is a funda-mentally different problem than that considered by Cheng et al. (1987) and by Killen and Morgan (1993, 1994), who treated Knud-sen flow from depth. Killen and Sarantos (2004) showed that the volatiles initially near the rims of grains are rapidly depleted, and that the rate at which a trace volatile is delivered to the extreme surface of a grain, where it can be acted upon by either photons or ions, is not only a function of temperature but also of grain size and time since the grain was first exposed to space weathering. In other words, there is a maximum ejection rate for a particular ele-ment set by the rate at which that element can diffuse to the ex-treme surface of the grain where it can desorb, and this rate is a function of grain size, phase (crystalline or amorphous), tempera-

ture, and weathering. We call this the diffusion-limited supply rate. Of course, meteoroid impacts can vaporize entire grains or boulders, depending on the impactor size, and this must be fac-tored into a global solution.

Fig. 9 shows that for a diffusion coefficient $D = 10^{-15}$ (cm^2 s^{-1}) all grains smaller than about 0.1 cm in radius will be able to supply the atmosphere at the required rate given by the known exosphere loss rate, assumed here to be 10^7 cm^{-2} s^{-1}, until half of their solute is lost. For progressively larger grains, a lesser fraction of solute will be lost at the required rate, and thereafter the rate will drop exponentially. This result is completely consistent with that of Kil-len (1989), who determined that diffusion out of glass grains is too fast and diffusion from a semi-infinite slab of crystalline mineral is too slow to maintain the exosphere. This is because small, hot grains, and glass grains, lose their volatiles rapidly, and large, crys-talline grains or a slab lose their volatiles at a much slower rate. For smaller values of the diffusion coefficient, progressively smaller grains will be unable to deliver their solute to the extreme surface at the required rate. One-centimeter-radius spheres can maintain a maximal thermal vaporization rate at the subsolar point (at perihe-lion) if they are glass. At aphelion, even mineral grains can main-tain the maximal thermal loss rate for the lifetime of the grain on the surface.

Given a fractal distribution of grain sizes, and a distribution of temperatures on the surface, on average the exosphere is main-tained at the observed rate (Killen and Sarantos, 2004). How does this explain the observed variability?

Boundaries on the diffusion coefficients for Na and K, respec-tively, are shown in Fig. 9 for glass from the leftmost boundary to the right-pointing arrow and for minerals from the rightmost boundary to the left-pointing arrow. Note that the expected K diffu-sion coefficients are in the region where the fraction of solute that will degas at a rate of 10^7 cm^{-2} s^{-1} is a steep function of the diffu-sion coefficient, D (and thus of temperature). Suppose that an event occurs that causes an increased yield of alkalis to the exosphere, such as a coronal mass ejection (e.g., Kallio and Janhunen, 2003). Fig. 9 shows that Na atoms will be able to fill holes created by
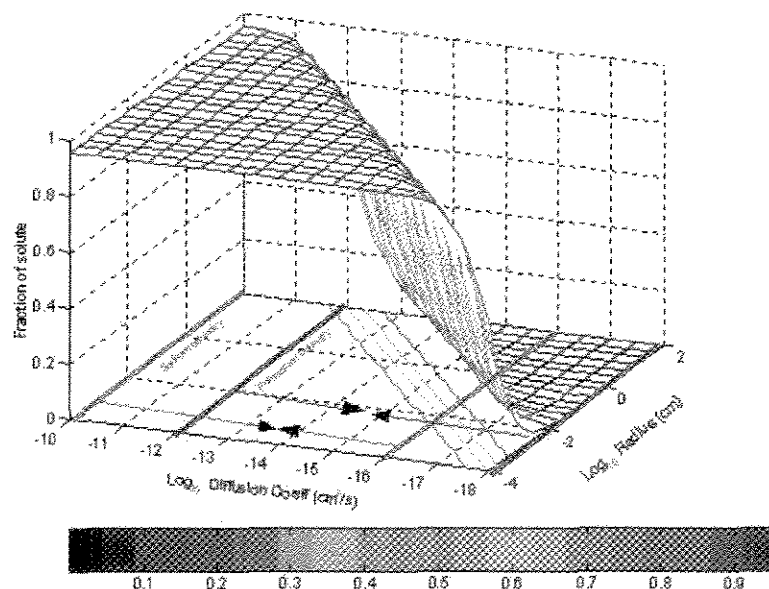

Fig. 9. The fraction of solute lost before the flux drops to 50% of the maximum for an initial rate of 10^7 cm^{-2} s^{-1} is plotted vs. radius and diffusion coefficient (from Killen and Sarantos, 2004). Limits on D for glassy grains are shown for sodium and potassium. Note that for K, a flux of 10^7 is much less likely to be maintained than for Na, since the diffusion coefficients for K at temperatures found at Mercury are on the steeply declining portion of the graph. This may explain the sensitivity of the Na/K ratio in the atmosphere to external forcing that is independent of surface temperature, such as ion sputtering.

desorption much more rapidly than will K atoms. All grains larger than 1 μm can supply Na at a rate of 10^7 cm^{-2} s^{-1}, but only grains larger than 100 μm can supply K at that rate. The fraction of solute lost per unit time at a given temperature is much greater for Na (pink boundary) than for K (blue boundary). The region of interest for Mercury is between the bold blue lines on the log diffusion coefficient scale for K and between the bold pink lines for Na. Thus, the Na/K ratio in the atmosphere may increase after an energetic event in which most surface atoms are desorbed because the Na sites will be rapidly refilled, but the K sites will take more time to recover.

5. Conclusions

The existence of very hot refractory species in Mercury's exosphere is consistent with ejection of molecules from the surface, with subsequent dissociation into hot fragments. The hot Mg tail is consistent with a surface abundance of 5–8% Mg, if 30% of impact-vaporized Mg remains as MgO at quenching and half of the impact vapor condenses. All of the ejected MgO molecules are assumed to be dissociated to populate the tail region with the observed hot atomic Mg. Globally, ion sputtering is not a major source of Mg, but locally the sputtered source may be comparable to or greater than the impact vapor source. Photons can desorb Mg from MgO, so PSD may be an important source for Mg on the dayside if MgO is deposited on the surface by some process such as impact vaporization of a regolith mineral. Mg has not been observed on the dayside of Mercury to date, and because of the sparsity of data we cannot determine the global distribution of Mg at this time. Nonetheless, the terminator data show that the temperature of the Mg gas decreases and the Mg number density at the surface increases as the dawn terminator is approached.

We conclude that the Na and K in Mercury's exosphere can be derived from a regolith composition similar to that Luna 16 lunar soil in which the abundances are 0.0027 for Na and 0.0006 for K (Heiken et al., 1991). The variability of Na and K in the exosphere is shown to be weakly correlated with the solar UV flux at Mercury with a correlation coefficient of 0.66. This variability of the Na/K ratio may be related to the differences in diffusion from the interiors of regolith grains to the extreme surface where they are ejected by PSD or ion sputtering. The variability in the exosphere is larger than local differences in the Na/K abundance, if they are similar to differences between Apollo orange glass and Luna 16 samples. Since Caloris basin was visible in the northern hemisphere between 23° and 58° from the sub-Earth longitude on the illuminated portion of the disk, and exospheric potassium was found to be weak in that region, we conclude that K is not enhanced over the Caloris basin at that time, in contrast to the findings of Sprague et al. (1990). Very large values of Na/K are indicative of small abundances of K and are influenced by noise.

Observations of Mg in the near-terminator region appear to show that the surface number density increases and the temperature of the gas decreases as the dawn hemisphere is approached. A single model does not match all of the data, indicating the existence of a non-uniform exosphere. New models of the Mercury magnetosphere derived from MESSENGER observations should make it possible to test loss and recycling rates. The newly discovered element in Mercury's exosphere, Mg, clearly is promoted into the exosphere by processes that are different from those ejecting the more volatile species, Na and K. Whereas the temperature of the volatile species, Na and K, has been shown to be approximately that expected for a PSD source, or 1200 K, the temperature found for Mg is on the order of tens of thousands of degrees. Na and K exist in an extended anti-sunward tail because they are accelerated by radiation pressure due to the strong resonance lines in the visible region of the solar spectrum. There is no such strong reso-

nance line for Mg in the visible region where the solar flux is strong; hence radiation pressure is negligible for Mg. Nevertheless we measured Mg in the anti-sunward tail. The conclusion is that the source process promoting Mg to the exosphere produces the hot Mg. This is very similar to the conclusion that we have found for Ca (Killen et al., 2005). These refractory species are ejected into the exosphere by a process that imparts ∼2 eV to the Mg atom and ∼3 eV to the Ca atom. We do not yet have enough data to determine the global distribution of Mg. However, the data shown herein indicate that the Mg is non-uniform.

Appendix A

The comparison of data to the Chamberlain model is achieved by first generating model predictions of the exosphere over a range of temperatures and densities along the line of sight for the observations. Then the model-predicted column abundances are compared to the data in a least squares analysis to retrieve the temperature and density. The analysis can be broken down into categories for each observation regime.

A.1. Tail-sweep observations

For the tail-sweep observations the spacecraft is not in the shadow of the planet. The line of sight oscillates up and down relative to the planet's equatorial plane, causing it to intersect the planet's shadow for some of the observations and not intersect the shadow for others. A subset of observations was selected where the lines of sight were pointing near the equatorial plane and passed through the shadow of the planet. Referring to Fig. 4, the column abundance along the portion of the line of sight in the dawn-side hemisphere, S_2, was calculated over a range of temperatures and densities using R_2 and θ_2 as inputs to the Chamberlain model and with S_2 extending from R_2 to infinity. The column abundance along the portion of the line of sight in the dusk-side hemisphere, S_1, was determined over a range of temperatures and densities by calculating the column abundance from R_1 to infinity in the direction of the spacecraft and from R_{sc} to infinity and then taking the difference between the two. A least squares analysis was performed over temperature and density for both the dusk-side and dawn-side lines of sight. For a single temperature, the Chamberlain-predicted column abundances from the dawn-side hemisphere for the entire range of densities were added one by one to each of the column abundances from the dusk-side hemisphere over their range of densities for the same temperature. This was done for each of the subset of observations and compared to the corresponding set of measured column abundances. The difference is

$$D(T, \rho_{dawn}, \rho_{dusk}) = \sum_{i=1}^{n} [N_i - M(T, \rho_{dawn}, \rho_{dusk})]^2 \qquad (A1)$$

where N is the measured column abundance, M is the model-predicted column abundance at a specific temperature (T), dawn-side density (ρ_{dawn}), and dusk-side density (ρ_{dusk}), and the sum is over the number of observations (n). The result is a three-dimensional matrix of D where the minimum value is interpreted as the best fit of the data to the model.

A.2. Fantail observations

When the spacecraft is in shadow, the line of sight can only exit the shadow. The column abundance was determined over a range of temperatures and densities along the line of sight from the point where it exits the planet's shadow to infinity. The fantail observations were analyzed by comparing all of the fantail data with the corresponding Chamberlain-predicted column abundances over temperature and density. The difference is given by

$$D(T, \rho) = \sum_{i=1}^{n} [N_i - M(T, \rho)]^2 \qquad (A2)$$

where N is the measured column abundance, M is the model-predicted column abundance at a specific temperature (T) and density (ρ), and the sum is over the number of observations (n). The result is a two-dimensional matrix of D where the minimum value is interpreted as the best fit of the data to the model.

A.3. Terminator observations

When the spacecraft is not in the planet's shadow but the field of view intersects the shadow and then intersects the planet, the Chamberlain column abundance over a range of temperatures and densities was calculated from the point of line-of-sight intersection with the shadow to infinity (this column will pass through the spacecraft) and from the spacecraft to infinity (this will be in the direction opposite to the line of sight). The second quantity was subtracted from the first, and the same least squares analysis was performed as for the fantail observations.

References

Benna, M., and 17 colleagues, 2010. Modeling of the magnetosphere of Mercury at the time of the first MESSENGER flyby. Icarus, in press. doi:10.1016/j.icarus2009.11.036.

Berezhnoy, A.A., Klumov, B.A., 2008. Impacts as sources of the exosphere of Mercury. Icarus 195, 511–522.

Bida, T.A., Killen, R.M., Morgan, T.H., 2000. Discovery of Ca in the atmosphere of Mercury. Nature 404, 159–161.

Borin, P., Cremonese, G., Marzari, F., Bruno, M., Marchi, S., 2009. Statistical analysis of micrometeoroids flux on Mercury. Astron. Astrophys. 503, 259–264.

Brown, M.E., 2001. Potassium in Europa's Atmosphere. Icarus 151, 190–195.

Burger, M.H., Killen, R.M., Vervack Jr., R.J., Bradley, T., McClintock, W.E., Sarantos, M., Benna, M., Mouawad, N., 2010. Monte Carlo modeling of sodium in Mercury's exosphere during the first two MESSENGER flybys. Icarus, submitted for publication.

Chamberlain, J.W., Hunten, D.M., 1987. Theory of Planetary Atmospheres. Academic Press, Orlando, FL. 481pp.

Cheng, A.F., Johnson, R.E., Krimigis, S.M., Lanzerotti, L.J., 1987. Magnetosphere, exosphere and surface of Mercury. Icarus 71, 430–440.

Cintala, M.E., 1992. Impact-induced thermal effects in the lunar and mercurian regoliths. J. Geophys. Res. 97, 947–973.

Fulle, M., Leblanc, F., Harrison, R.A., Davis, C.J., Eyles, C.J., Halain, J.P., Howard, R.A., Bockelee-Morvan, D., Cremonese, G., Scarmato, T., 2007. Discovery of the atomic iron tail of Comet McNaught using the heliospheric imager on STEREO. Astrophys. J. 661, L93–L96.

Gault, W.A., Rundle, H.N., 1969. Twilight observations of upper atmospheric sodium, potassium, and lithium. Can. J. Phys. 47, 85–98.

Hayderer, G., and 11 colleagues, 2001. Kinetically assisted potential sputtering of insulators by highly charged ions. Phys. Rev. Lett. 86, 3530–3533.

Heiken, G., Vaniman, D., French, B.M., 1991. Lunar Sourcebook: A User's Guide to the Moon. Cambridge Univ. Press. 736pp.

Hine, K., Yoshimura, S., Kazumaska, I., Kiuchi, M., Hashimoto, J., Terauchi, M., Nishitani, M., Hamaguchi, S., 2007. Measurement of magnesium oxide sputtering yields by He and Ar ions with a low-energy mass-selected ion beam system. Jpn. J. Appl. Phys. 46, L1132–L1134.

Huebner, W.F., Keady, J.J., Lyon, S.P., 1992. Solar photo rates for planetary atmospheres and atmospheric pollutants. Astrophys. Space Sci. 195, 1–294.

Joly, A., 2002. Femtosecond time-resolved photon-stimulated desorption from ionic crystals. Appl. Surface Sci. 186, 339–344.

Kallio, E., Janhunen, P., 2003. Solar wind and magnetospheric ion impact on Mercury's surface. Geophys. Res. Lett. 30, SSC 2.1–2.4. doi: 10.1029/2003GL017842.

Kallio, E., and 10 colleagues, 2008. On the impact of multiply charged heavy solar wind ions on the surface of Mercury, the Moon and Ceres. Planet. Space Sci. 56, 1506–1516.

Killen, R.M., 1989. Crustal diffusion of gases out of Mercury and the Moon. Geophys. Res. Lett. 16, 171–174.

Killen, R.M., Morgan, T.H., 1993. Diffusion of Na and K in the uppermost regolith of Mercury. J. Geophys. Res. 98, 23589–23601.

Killen, R.M., Morgan, T.H., 1994. Erratum: Diffusion of Na and K in the uppermost regolith of Mercury [J. Geophys. Res. 98, 23589–23601]. J. Geophys. Res. 99, 10937.

Killen, R.M., Sarantos, M., 2004. Source rates and ion recycling rates for Na and K in Mercury's atmosphere. Icarus 171, 1–19.

Killen, R.M., Potter, A.E., Morgan, T.H., 1990. Spatial distribution of sodium vapor in the atmosphere of Mercury. Icarus 85, 145–167.

Killen, R.M., Potter, A.E., Reiff, P., Sarantos, M., Jackson, B.V., Hick, P., Giles, B., 2001. Evidence for space weather at Mercury. J. Geophys. Res. 106, 20509–20525.

Killen, R.M., Bida, T.A., Morgan, T.H., 2005. The calcium exosphere of Mercury. Icarus 173, 300–311.

Killen, R.M., Shemansky, D.E., Mouawad, N., 2009. Expected emission from Mercury's exospheric species, and their UV-visible signatures. Astrophys. J. Suppl. 181, 351–359.

Kurucz, R.L., Furenlid, I., Brault, J., Testerman, L., 1984. Solar Flux Atlas from 296 to 1300 nm. National Solar Observatory Atlas No. 1, Tucson, Ariz.

Lodders, K., Fegley Jr., B., 1998. The Planetary Scientist's Companion. Oxford Univ. Press, New York. 371pp.

Love, S.G., Brownlee, D.E., 1993. A direct measurement of the terrestrial mass accretion rate of cosmic dust. Science 262, 550–553.

Madey, T.E., Yakshinskiy, B.V., 1997. Desorption of Na from model mineral surfaces: Relevance to origins of Na in the atmospheres of Mercury and the Moon. Bull. Am. Astron. Soc. #13.07 (abstract) 29, 987.

Madey, T.E., Yakshinskiy, B.V., Ageev, V.N., Johnson, R.E., 1998. Desorption of alkali atoms and ions from oxide surfaces: Relevance to origins of Na and K in the atmospheres of Mercury and the Moon. J. Geophys. Res. 103, 5873–5887. doi:10.1029/98JE00230.

McClintock, W.E., Lankton, M.R., 2007. The Mercury Atmospheric and Surface Composition Spectrometer for the MESSENGER mission. Space Sci. Rev. 131, 481–521.

McClintock, W.E., Vervack Jr., R.J., Bradley, E.T., Killen, R.M., Mouawad, N., Sprague, A.L., Burger, M.H., Solomon, S.C., Izenberg, N.R., 2009. MESSENGER observations of Mercury's exosphere: Detection of magnesium and distributions of species. Science 324, 610–613.

Melosh, H.J., 1989. Impact Cratering – A Geologic Process. Oxford University Press. 253pp.

Morgan, T.H., Killen, R.M., 1998. Production mechanisms for faint but possibly detectable coronae about asteroids. Planet. Space Sci. 46, 843–850.

Morgan, T.H., Zook, H.A., Potter, A.E., 1988. Impact-driven supply of sodium and potassium to the atmosphere of Mercury. Icarus 75, 156–170.

Murthy, N.S., Bagare, S.P., 1978. Dissociation energy of MgO from the true potential curve. J. Phys. B: At. Mol. Phys. 11, 623–626.

Nyquist, L.E., Wooden, J., Bansal, B., Weismann, H., McKay, G., Bogard, D.D., 1979. Rb–Sr age of the Shergotty achondrite and implications for metamorphic resetting of isochron ages. Geochim. Cosmochim. Acta 43, 1057–1074.

Potter, A.E., Morgan, T.H., 1988. Discovery of sodium and potassium vapor in the atmosphere of the moon. Science 241, 675–680.

Potter, A.E., Morgan, T.H., 1997. Sodium and potassium atmospheres of Mercury. Planet. Space Sci. 45, 95–100.

Potter, A.E., Anderson, C.M., Killen, R.M., Morgan, T.H., 2002. Ratio of sodium to potassium in the Mercury exosphere. J. Geophys. Res. 107, 5040. doi:10.1029/2000JE001493.

Ralchenko, Yu., Kramida, A.E., Reader, J., and the NIST ASD Team, 2008. NIST Atomic Spectra Database (online). National Institute of Standards and Technology, Gaithersburg, Md.

Roth, J., 1983. Chemical sputtering. In: Behrisch, R. (Ed.), Sputtering by Particle Bombardment II. Springer-Verlag, New York, pp. 91–141.

Sarantos, M., 2005. Ion Trajectories in Mercury's Magnetosphere. Ph.D. Dissertation, Rice University Publication AAT 3176074, Houston, 81pp.

Sarantos, M., Killen, R.M., Kim, D., 2007. Predicting the long-term solar wind ion-sputtering source at Mercury. Planet. Space Sci. 55, 1584–1595.

Snow, M., Woods, T.N., Eparvier, F.G., Fontenla, J., Harder, J., McClintock, W.E., and the LISIRD Team, 2005. The LASP Interactive Solar Irradiance Datacenter (LISIRD). Eos Trans. Am. Geophys. Union (Fall Suppl.) 86 (52). Abstract IN-33B-1180.

Southworth, R.B., Sekinina, Z., 1973. Physical and Dynamical Studies of Meteors. NASA CR-2316.

Sprague, A.L., Kozlowski, R.W.H., Hunten, D.M., 1990. Caloris basin: An enhanced source for potassium in Mercury's atmosphere. Science 249, 1140–1143.

Wang, W.-M., 2008. Relating the solar wind helium abundance to the coronal magnetic field. Astrophys. J. 683, 499–509.

Yakshinskiy, B.V., Madey, T.E., 1999. Photon-stimulated desorption as a substantial source of sodium in the lunar atmosphere. Nature 400, 642–644.

Yakshinskiy, B.V., Madey, T.E., 2004. Photon-stimulated desorption of Na from a lunar sample: Temperature-dependent effects. Icarus 168, 53–59.

Yakshinskiy, B.V., Madey, T.E., 2005. Temperature-dependent DIET of alkalis from SiO_2 films: Comparison with a lunar sample. Surface Sci. 593, 202–209.